Computers in Biology and Medicine 110 (2019) 15–28

Contents lists available at ScienceDirect

Computers in Biology and Medicine

journal homepage: www.elsevier.com/locate/compbiomed

An image reconstruction method for endoscopic photoacoustic tomography in tissues with heterogeneous sound speed

Sun Zheng*, Jia Yixuan

Department of Electronic and Communication Engineering, North China Electric Power University, Baoding, 071003, China

ARTICLE INFO

Keywords:
Endoscopic photoacoustic tomography (EPAT)
Speed of sound (SOS)
Acoustic heterogeneity
Image reconstruction
Optical deposition

ABSTRACT

The idealized assumption of a constant speed of sound (SOS) in acoustically inhomogeneous biological tissues usually results in blurred details, acoustic distortion and artifacts in *in vivo* endoscopic photoacoustic tomographic (EPAT) images. In this paper, we propose an image reconstruction method to improve EPAT imaging for luminal structures with the variable SOS. In our method, an optimal SOS providing the maximal local focusing of a measuring location within the imaging region is firstly determined. The deviation in the ultrasonic propagation time caused by the variable SOS is then compensated. The grayscale images of the optical absorption distribution on the cross-sections of the luminal structures are finally reconstructed with a filtered back-projection (FBP) algorithm based on the corrected propagation time. Any prior knowledge of the SOS distribution in the imaged tissues is not required. The results of numerical simulation experiments demonstrated that the proposed method can effectively improve the image quality by reducing the misalignment of tissues, acoustic distortion and artifacts caused by the variable SOS.

1. Introduction

1.1. Background

Photoacoustic tomography (PAT) is capable of visualizing the optical absorption of biological tissues by combining the high contrast of purely optical imaging techniques with the good spatial resolution of ultrasonography in deep tissues [1]. Endoscopic PAT (EPAT) combines PAT with endoscopic detection to visualize the morphology and functional components of the luminal structures from the inside [2,3]. Grayscale images of the optical deposition displaying the cross-sectional morphology can be recovered from the time-dependent boundary measurements of the photoacoustic (PA) pressure [4,5]. Furthermore, the distribution of the optical absorption coefficient and scattering coefficient can also be recovered according to which the functional components of the tissues are quantitatively evaluated and analyzed [6].

For simplicity, the standard algorithms for reconstructing PAT images are usually based on an idealized assumption of a constant speed of sound (SOS) within the imaged tissues [4,7]. Previous experiments have demonstrated that such an assumption is reasonable for a weak variation in the SOS or for a small scanning geometry of the imaged target relative to the ultrasonic detector [8]. Actually, the spatial variation in the acoustic properties of human organs with different chemical compositions is usually unknown before *in vivo* PAT imaging. The variation in the SOS in soft tissues can even reach 10%. For example, the SOS varies from 1400 m/s to 1450 m/s in subcutaneous tissue, ranges from 1500 m/s to 1560 m/s in normal parenchyma and stroma and 1600 m/s in muscle [9,10]. In the case of a strong variation in the SOS, such an assumption may lead to computational errors in the time of the ultrasonic waves propagating from the acoustic source to the ultrasonic transducer. Further, the distance between the acoustic source and the ultrasonic transducer calculated according to this time is also incorrect. It subsequently results in acoustic distortion, significant artifacts, blurred details and tissue misalignment in the reconstructed images. Especially, serious acoustic distortion may occur and even some tissues cannot be imaged in those regions where the SOS of the system mismatches that of the tissues seriously, such as bones or lungs [9].

1.2. Related work

The prior properties of the acoustic inhomogeneity of tissues which is usually necessary to achieve high-quality reconstruction is hard to obtain before *in vivo* PAT applications. To reduce image artifacts and correct the acoustic distortion, some image reconstruction algorithms

* Corresponding author. Postal address: P.O. Box 21, North China Electric Power University, Baoding 071003, China.
E-mail address: sunzheng_tju@163.com (S. Zheng).

https://doi.org/10.1016/j.compbiomed.2019.05.008
Received 7 February 2019; Received in revised form 5 May 2019; Accepted 8 May 2019
0010-4825/ © 2019 Elsevier Ltd. All rights reserved.

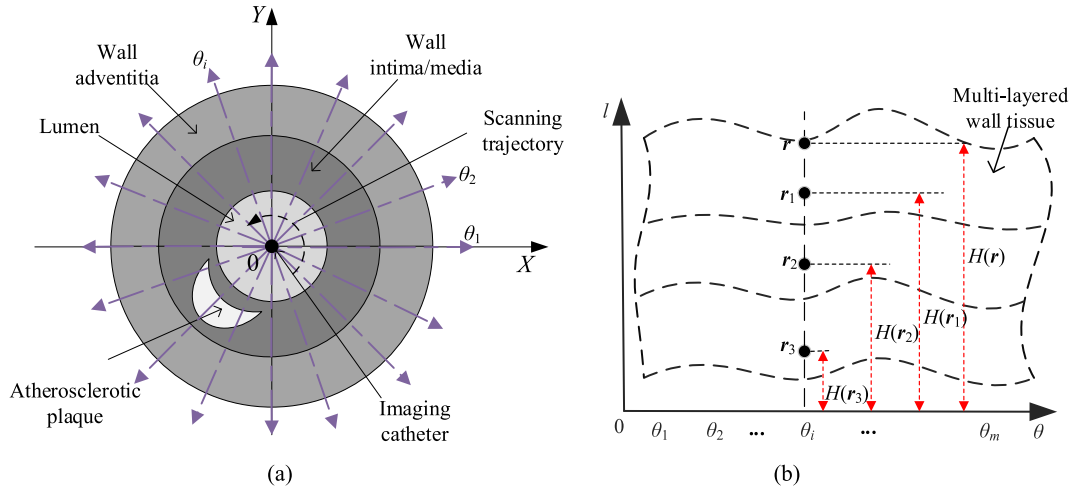

Fig. 1. Schematics of IVPAT imaging geometry on a coronary arterial cross-section. (a) Measuring angles in a planar rectangular coordinate system *XOY*; (b) Multi-layered wall tissues in a *θ-l* polar coordinate system.

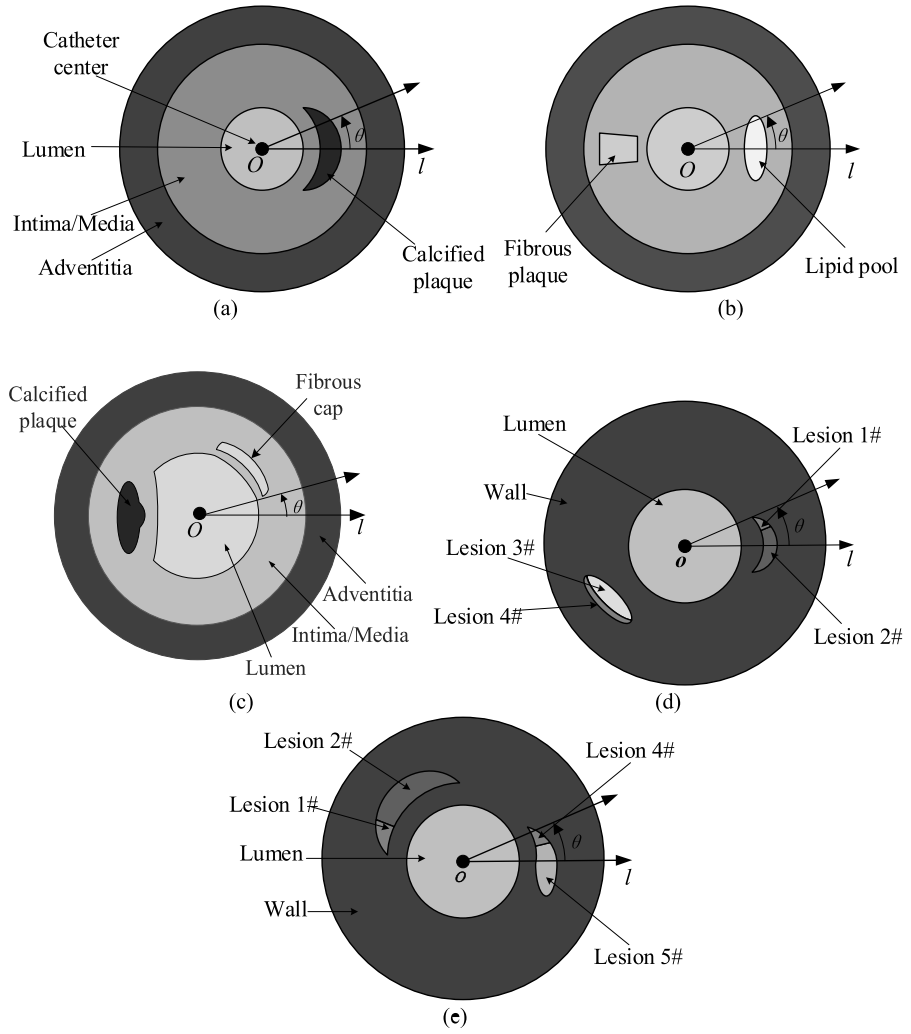

Fig. 2. Cross-sectional geometry of computer-simulated phantoms. (a) Vessel phantom 1#; (b) Vessel phantom 2#; (c) Vessel phantom 3#; (d) Cavity phantom 1#; (e) Cavity phantom 2#.

assume that the SOS varies continuously in the same tissue and changes abruptly between different tissues. The SOS distribution of the tissue boundaries is assumed to be consistent with that of the optical absorption distribution [11]. Besides, several fixed sound speeds are assumed in case of low accuracy requirement [12]. A more accurate method is to quantitatively measure the SOS distribution before PAT by using ultrasound transmission tomography (UTT) [13,14]. But, the UTT-based methods require additional equipment and imaging

Table 1
Geometrical, optical and acoustic parameters of vessel phantoms.

Tissue name	Composition	Average refractive index	Absorption coefficient (cm^{-1})	Scattering coefficient (cm^{-1})	Anisotropy factor	Average SOS (m/s)	Density (kg/L)	Radial thickness (mm)	
								Vessel 1# and 2#	Vessel 3#
Adventitia	Connective tissue	1.41	0.20	5	0.80	1600	1.016	1.3	1
Intima/Media	Muscular tissue	1.41	0.20	5	0.80	1580	1.070	2.4	1.7–2.0
Calcified plaque	Calcium	1.46	0.60	550	0.80	1650	1.658	0.5–0.8	
Fibrous plaque	Fibrous tissue	1.46	0.01	20	0.75	1610	1.048	0.8	–
Fibrous cap	Fibrous tissue	1.46	0.03	80	0.75	1610	1.048	–	0.2
Lipid pool	Lipid	1.46	0.10	500	0.80	1480	0.937	0.5	–
Lumen	Blood	1.34	0.70	600	0.99	1560	1.055	1.2	1.0–1.3

Table 2
Geometrical, optical and acoustic parameters of cavity phantoms.

Tissue name	Composition	Average refractive index	Absorption coefficient (cm^{-1})	Scattering coefficient (cm^{-1})	Anisotropy factor	Mean SOS (m/s)	Density (kg/L)	Radial thickness (mm)
Wall	Connective/Muscular tissue	1.42	0.20	15	0.80	1600	1.016	6.5
Lesion 1#	Effusion	1.46	0.10	300	0.75	1620	1.085	2.5
Lesion 2#	Tumour	1.47	0.02	50	0.80	1630	1.102	3.6
Lesion 3#	Fatty tissue	1.46	0.10	500	0.80	1480	0.937	2.5
Lesion 4#	Fibrous tissue	1.46	0.01	20	0.75	1610	1.048	1.3
Lesion 5#	Fibro-fatty tissue	1.46	0.02	30	0.80	1500	0.992	3.2
Lumen	Digestive juice	1.00	0.50	600	0.99	1560	1.003	5.6

procedures, which may increase the operating complexity and prolong the imaging time.

Several methods have been proposed to effectively improve the reconstruction quality by incorporating the SOS distribution into the reconstruction. For example, in the case of PAT imaging in soft tissues with the SOS variation lower than 10%, the approximate time of the ultrasonic waves propagating between two spatial points is estimated according to the correlation between the signals detected at different locations [15]. Although any prior knowledge of the SOS distribution is not needed, the target to be measured is required to be small relative to the detector and the detector should be far away from the target. Another similar method presented in [16] compensates for the delay error in the ultrasonic propagation time by fitting the relationship of the delay compensation relative to the detection depth. The in-focus region is only in a certain depth causing defocusing at other depths with a fixed delay. Thereby, various delay compensation values are needed to achieve accurate reconstruction, leading to the high computational cost and complexity of the system.

The method based on auto-focusing [17], optimal focusing [18] or maximizing coherence factor [10] automatically selects a proper SOS in a region of interest (ROI) through maximizing the sharpness of the local image features or minimizing the absolute difference of the focused PA signal. It is computationally efficient and can improve the image contrast and spatial resolution. However, it needs the prior knowledge of the rough location of the target tissues. And, the computational time depends on the ROI size. Besides, the optimal SOS group method recursively updates the initial SOS group through maximizing the image focusing [19,20] in order to optimally match the SOS in different tissues. But, it is time-consuming and laborious to manually set initial plans and to find the optimal SOS through a large number of experiments.

TR is the standard approach for PAT reconstruction with variable SOS. The SOS distribution is iteratively updated from an initial plan by using the time reversal mirror (TRM) and simultaneous algebraic reconstruction technique (SART) [21,22]. Another improved approach estimates the tissue region with or without the variable SOS based on the ultrasonic time-of-flight (TOF) in order to select the optimal TOF implying the acoustic heterogeneity [23]. It is computationally efficient because it chooses the optimal TOF instead of all TOFs to estimate the SOS distribution.

The full-wave analysis is an alternative iterative method of PAT reconstruction with variable SOS [24–27]. A discrete imaging model is established based on the exact solutions to the PA wave equation. The forward operator and backprojection operator are obtained by using the *k*-space pseudospectral method. Then, the distribution of the initial acoustic pressure or optical absorption is reconstructed by iteratively solving the regularized partial least square problem. Full-wave analysis is more efficient in compensating for the acoustic aberration and reducing image artifacts compared with the finite difference method. But, it usually requires more iterations and the reconstruction accuracy is susceptible to the noises in the PA measurements.

Finite element methods (FEMs) [28,29] solve the Helmholtz wave equation with the second-order absorbing boundary conditions to obtain the theoretical acoustic pressure. Then, the distribution of the SOS and optical absorption is reconstructed through iteratively updating the optical and acoustic coefficients and minimizing the mean square error between the measured and theoretical acoustic pressure. The FEM-based reconstruction is computationally burdensome caused by the complicated and excessive repetitive computation.

Alternating optimization method [30] establishes a discrete forward model related to the distribution of the SOS and the optical absorption according to the time-domain PA wave equation. Then, two penalized least square problems are alternately solved, that is, reconstructing the optical absorption distribution according to the given SOS and reconstructing the SOS distribution according to the given optical absorption. However, it is difficult to accurately estimate the SOS distribution only from the PA measurements even in the case of a complete data set. Other measurements are still required to improve the accuracy.

1.3. Objectives of the work

The primary objective of this work is to present a method to reconstruct EPAT images of luminal structures with variable SOS, such as

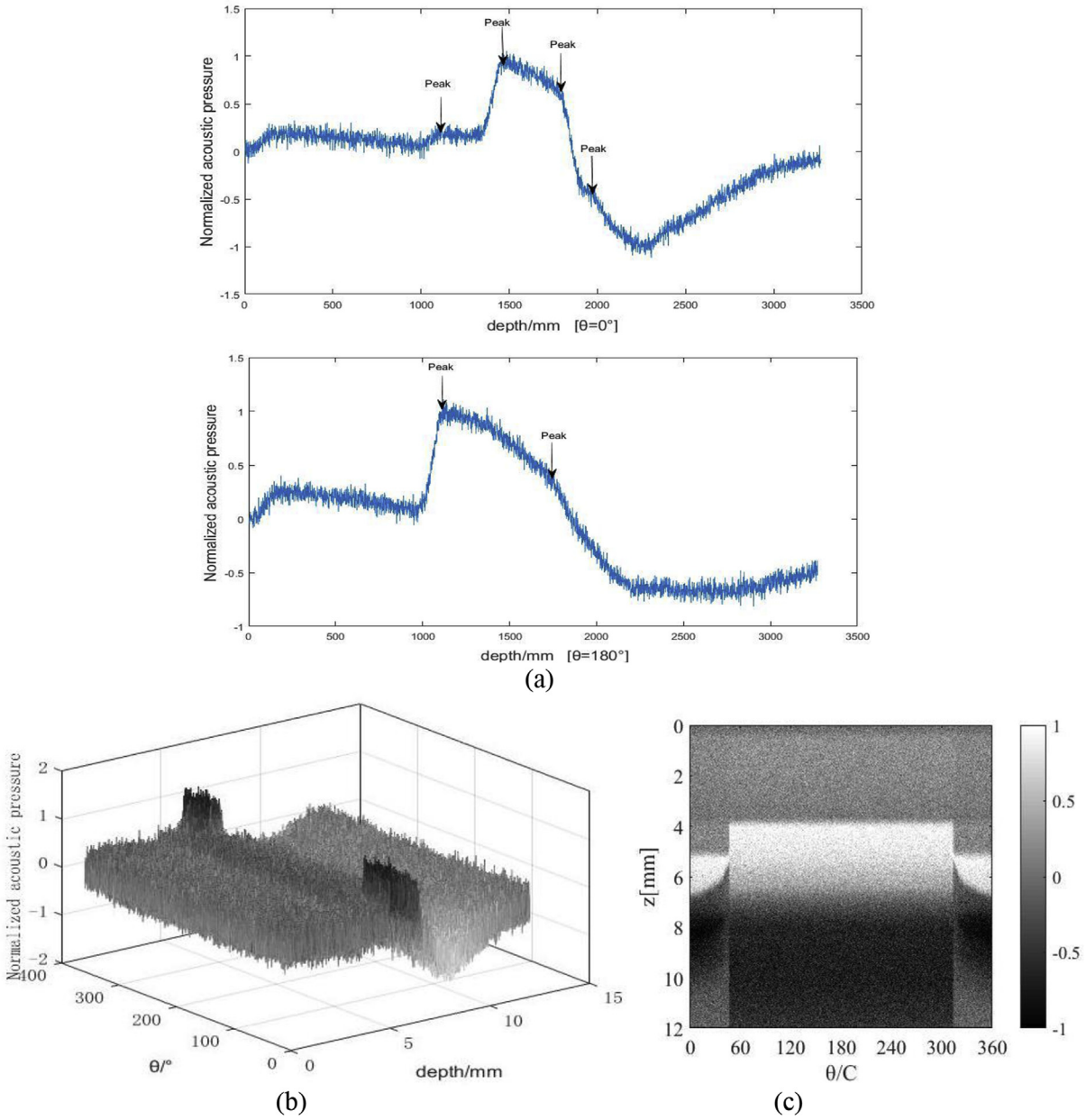

Fig. 3. Simulated PA signals of vessel phantom 1#. (a) Normalized acoustic pressure in the direction of 0° and 180°; (b) Full-view normalized acoustic pressure; (c) Polar view of the acoustic pressure distribution.

coronary arterial vessels and digestive tracts. The initial optical absorption distribution is firstly reconstructed from the PA boundary measurements based on a series of fixed sound speeds. Then, the deviation of the ultrasonic propagation time is calculated according to the optimal SOS providing the maximal local focusing. Further, the relationship of the temporal deviation of any measuring location in the imaging region relative to the radial depth on a cross-section of the target is fitted. Finally, the image of the optical absorption distribution on the cross-section is recovered based on the corrected time of the ultrasonic wave propagating between each measuring location and the ultrasonic detector. Any prior knowledge of the SOS distribution is not required. Computer-simulation experiments were conducted to demonstrate the validity of the method and to quantitatively evaluate the reconstruction quality and accuracy. Comparison experiments were conducted to compare the difference between the reconstructed images before and after variable SOS compensation. Additionally, numerical experiments were conducted that reveal the dependence of the reconstruction quality on the initial sound speeds and the temporal deviation. Comparison experiments between the proposed method and the optimal SOS group method were also provided.

The paper is organized as follows. Section 2 describes the proposed approach for solving the EPAT image reconstruction in tissues with variable SOS. The computer-simulation methodology and demonstration results are given in Section 3. Related discussions are given in Section 4. The paper concludes with a summary in Section 5.

2. Method

Intravascular photoacoustic tomography (IVPAT), a typical application of EPAT in the clinical diagnosis of coronary artery diseases, is taken as an example to illustrate the cross-sectional imaging geometry as shown in Fig. 1. The imaging catheter is located in the center of the vascular lumen. From inside to outside, the lumen, atherosclerotic plaques, vessel wall intima/media and adventitia are surrounding the

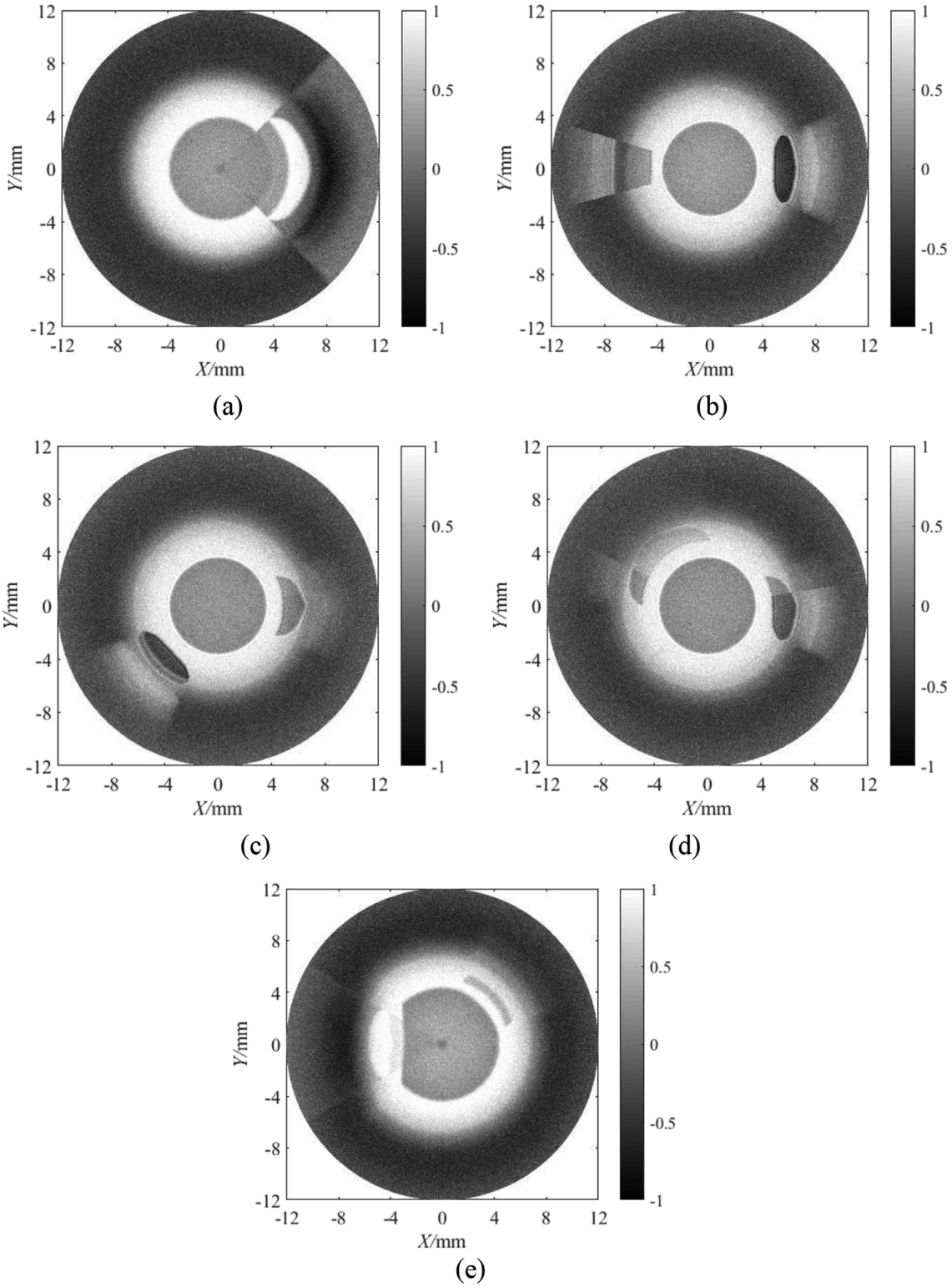

Fig. 4. Transverse view of the acoustic pressure distribution map. (a) Vessel 1#; (b) Vessel 2#; (c) Vessel 3#; (d) Cavity 1#; (e) Cavity 2#.

catheter. A single-element ultrasonic transducer mounted on the catheter tip collects the PA waves generated by the multi-layered vessel wall tissues when it circumferentially scans the surrounding tissues. For simplicity, an ideal point-like detector is assumed neglecting the aperture effect. The circular scanning trajectory is parallel to the image plane. A rectangular coordinate system with the origin of the catheter center is established (Fig. 1a). The vascular cross-section is equally divided into m sectors and the ith measuring angle is represented as $\theta_i = 360(i–1)/m$, where $i = 1,2, \ldots,m$. In Fig. 1b, a θ–l polar coordinate system is located at the catheter center, where θ is the polar angle and l is the polar radius representing the radial thickness of the multi-layered wall tissues. The internal wall surface is parallel to θ-axis and perpendicular to l-axis.

The acoustic waves propagating in the wall tissues satisfy the PA wave equation as follows,

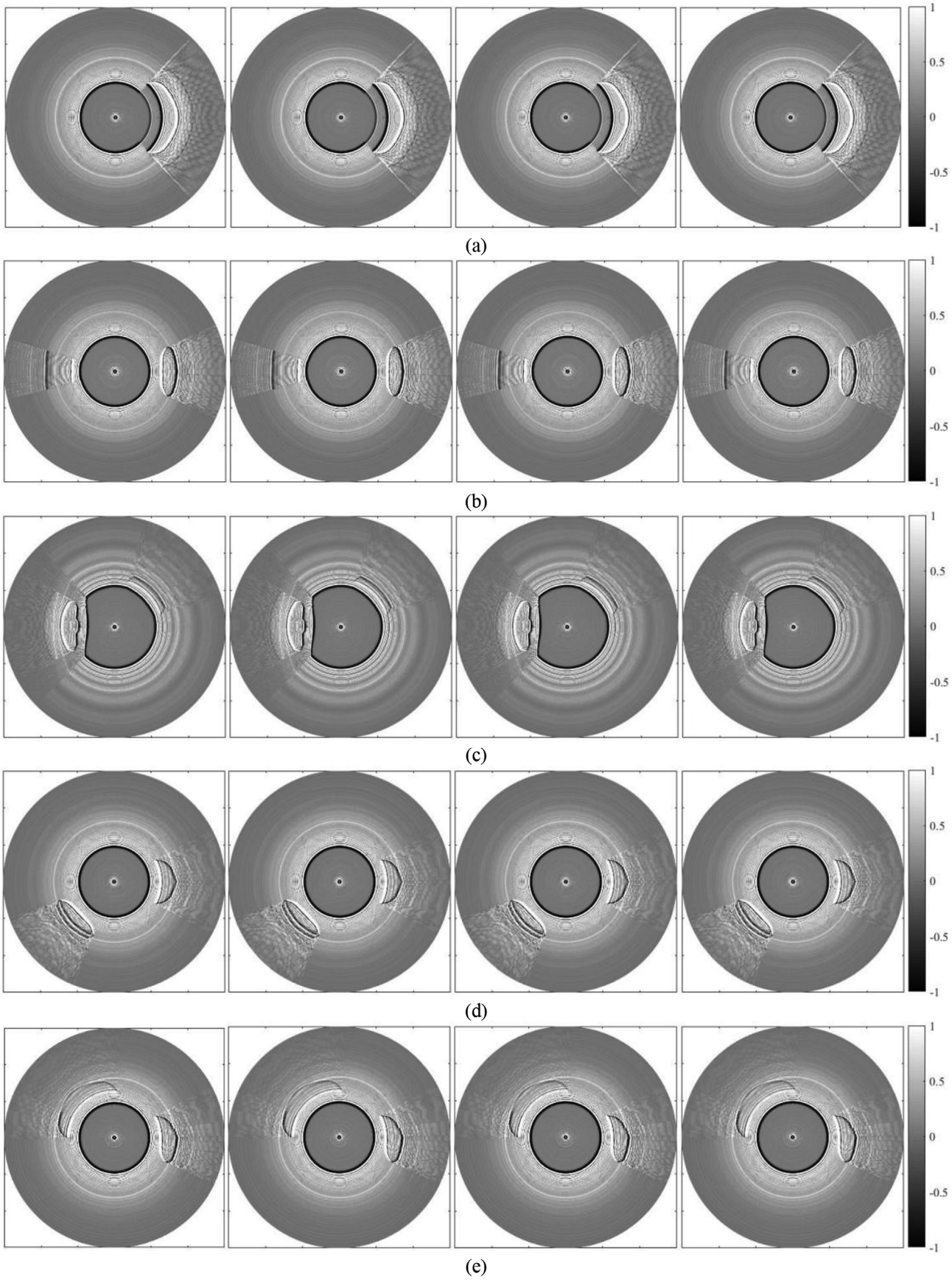

Fig. 5. Initial reconstruction with fixed sound speeds. In each subfigure, from left to right, the SOS is 1450 m/s, 1550 m/s, 1600 m/s and 1650 m/s, respectively. (a) Vessel 1#; (b) Vessel 2#; (c) Vessel 3#; (d) Cavity 1#; (e) Cavity 2#.

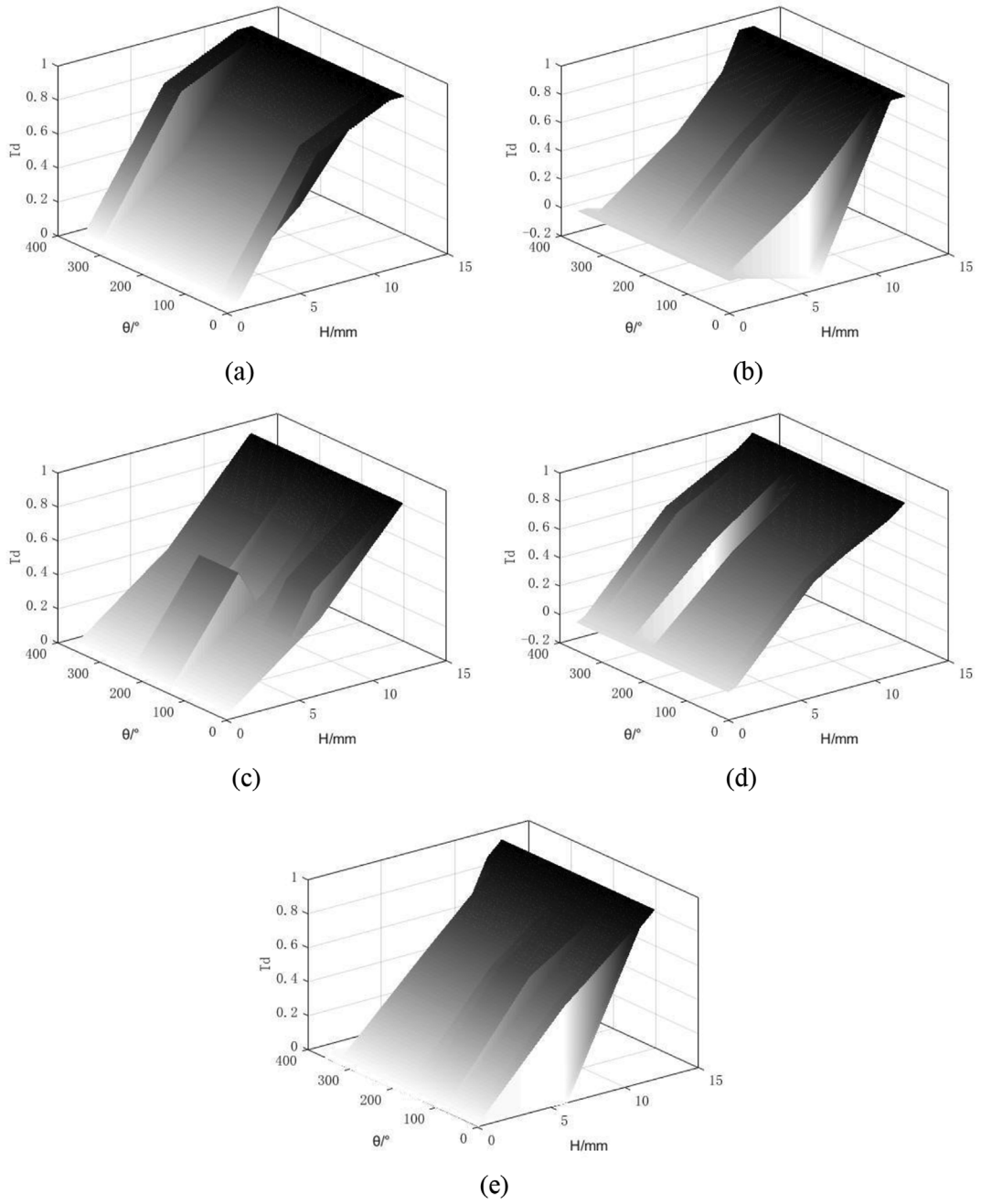

Fig. 6. Variation curve of the temporal deviation relative to the radial depth in the direction of 0°~360°. (a) Vessel 1#; (b) Vessel 2#; (c) Vessel 3#; (d) Cavity 1#; (e) Cavity 2#.

$$\nabla^2 p(\boldsymbol{r}, t) - \frac{1}{[c(\boldsymbol{r})]^2}\frac{\partial^2 p(\boldsymbol{r}, t)}{\partial t^2} = -\frac{\beta}{C_p}A(\boldsymbol{r})\delta'(t), \tag{1}$$

where $\boldsymbol{r}$ is a measuring location in the imaging region, $p(\boldsymbol{r}, t)$ represents the acoustic pressure at $\boldsymbol{r}$ and time t, β is the isobaric expansion coefficient, C_p is the specific heat, $A(\boldsymbol{r})$ is the absorbed optical energy at $\boldsymbol{r}$, $c(\boldsymbol{r})$ is the SOS at $\boldsymbol{r}$, $\delta(t)$ is the instantaneous laser pulse function with zero pulse emission time, and $\delta'(t)$ is the first-order derivative of $\delta(t)$ relative to t. In the case of a fixed SOS, $A(\boldsymbol{r})$ can be solved by using a standard filtered back-projection (FBP) algorithm [31] as follows,

$$A(\mathbf{r}) = -\frac{4C_p}{\beta c_s^3}\sum_{i=1}^{m}\frac{H(\mathbf{r})}{|\mathbf{r}_i - \mathbf{r}|}\frac{1}{t}\frac{\partial p_i(t)}{\partial t}\bigg|_{t=\frac{|\mathbf{r}_i-\mathbf{r}|}{c_s}}, \tag{2}$$

where c_s is the fixed SOS, $H(\boldsymbol{r})$ is the radial depth, i.e., the vertical distance between the location $\boldsymbol{r}$ and θ-axis as shown in Fig. 1b, and $p_i(t)$ is the acoustic pressure measured at time t in the direction of θ_i.

We assume that the wall tissues including plaques and lesions have a weak acoustic heterogeneity. That is, the variation in the SOS is lower than 10%. A series of initial sound speeds ranging from 1450 m/s to 1650 m/s, are set, i.e., $c_0 = 1450$, $c_1 = 1450 + \Delta c$, $c_2 = 1450 + 2\Delta c$, ……, $c_N = 1450 + N\Delta c$, where Δc is the step. A series of polar views of the initial optical absorption distribution map, $\{A_0, A_1, \ldots\ldots, A_N\}$, are recovered according to eq. (2) where $c_s = c_0, c_1, \ldots\ldots, c_N$ respectively. The transverse views, $\{I_0, I_1, \ldots\ldots, I_N\}$, are then obtained through the coordinate transformation.

The local sharpness of the image features in $\{I_i | i = 0,1 \ldots\ldots,N\}$ is quantitatively measured with a local focusing metric [17],

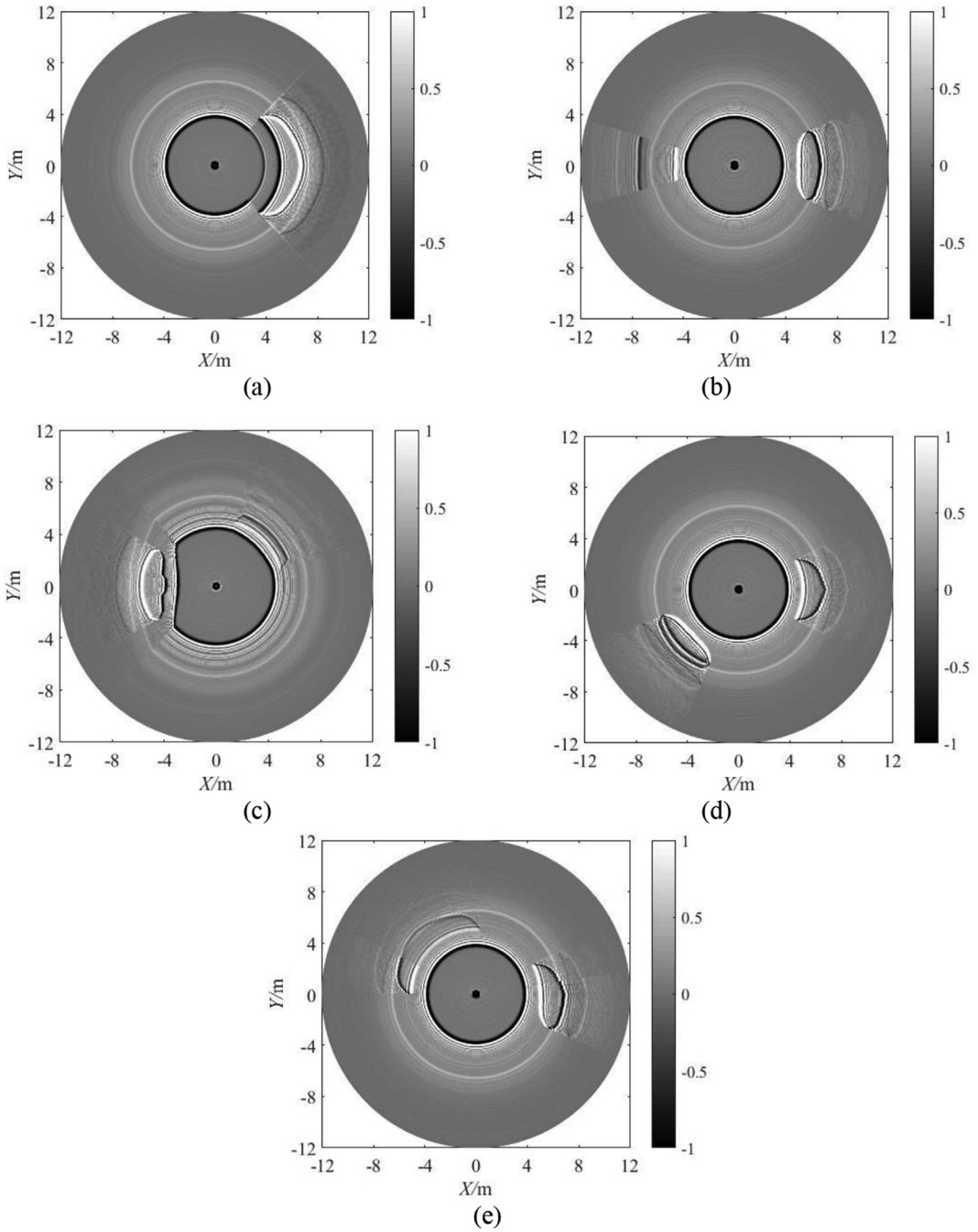

Fig. 7. Reconstructions after compensation for the variable SOS. (a) Vessel 1#; (b) Vessel 2#; (c) Vessel 3#; (d) Cavity 1#; (e) Cavity 2#.

$$F_i(x,y) = \sum_{j=-1}^{1}\sum_{k=-1}^{1}[g(j+1,k+1)I_i(x+k,y+j)]^2 + \sum_{j=-1}^{1}\sum_{k=-1}^{1}[g^{\mathrm{T}}(j+1,k+1)I_i(x+k,y+j)]^2, \quad (3)$$

where $i = 0,1,2,\ldots,N$, $I_i(x,y)$ is the grayscale of the pixel (x,y) in I_i, and $g(\cdot)$ is the Sobel operator. The maximum is selected from $\{F_i(x,y)|i = 0,1\ \ldots\ldots,N\}$, which is represented as $F_{\max}(x,y)$. The corresponding transverse map of the initial optical absorption distribution is represented as I_{opt} and the fix SOS being used to reconstruct I_{opt} is represented as c_{opt}.

The temporal deviation of the acoustic waves propagating from the location $\boldsymbol{r}$ to the ultrasonic detector is determined by

$$\Delta T(\boldsymbol{r}) = \frac{|\boldsymbol{r}-\boldsymbol{r}_0|}{c_0} - \frac{|\boldsymbol{r}-|_0|}{c_{\mathrm{opt}}}, \quad (4)$$

where $\boldsymbol{r}_0$ is the location of the detector. Because of the variable SOS, the temporal deviation varies with the radial depth as shown in Fig. 1b,

$$\Delta T(\boldsymbol{r}) = f(H(\boldsymbol{r})). \quad (5)$$

In this preliminary study, the function $f(\cdot)$ is simplified to a linear relationship [16] as follows,

$$\Delta T(\boldsymbol{r}) \approx C_0 + C_1 H(\boldsymbol{r}). \quad (6)$$

The linear coefficients, C_0 and C_1, are fitted from M pairs of the temporal deviation and the radial depth, $\{(\Delta T(\boldsymbol{r}_1), H(\boldsymbol{r}_1)), (\Delta T(\boldsymbol{r}_2), H(\boldsymbol{r}_2)), \ldots, (\Delta T(\boldsymbol{r}_M), H(\boldsymbol{r}_M))\}$, by using the least square method. Thus, using eq. (6), the temporal deviation of any measuring position can be achieved.

The optical absorption of the location $\boldsymbol{r}$ after correcting the propagation time is finally recovered as follows,

Table 3
NMSAD of the images reconstructed with our method and standard FBP with a fixed SOS.

		Vessel 1#	Vessel 2#	Vessel 3#	Cavity 1#	Cavity 2#
Standard FBP with a fixed SOS (*m/s*)	1500	4.914121	5.387642	5.064530	5.934547	6.047096
	1560	4.954872	5.427590	5.034981	5.955778	6.050956
	1570	4.967096	5.436759	5.031677	5.957771	6.056801
	1580	4.979981	5.427156	5.021202	5.923578	6.056020
	1590	4.991820	5.446578	5.027626	5.908797	6.060150
	1600	5.005389	5.508967	5.019670	5.906453	6.068152
	1610	5.014438	5.515087	5.008231	5.957032	6.070150
	1620	5.021675	5.589056	5.027659	5.909786	6.075016
	1630	5.030600	5.532907	5.048726	6.000760	6.079214
	1640	5.030091	5.545697	5.067903	6.009467	6.080678
	1650	5.084367	5.536714	5.089234	6.012436	6.081658
Our method		4.754890	4.943987	4.792103	5.665411	5.605880

$$A(\mathbf{r}) = -\frac{4C_p}{\beta c_0^3}\sum_{i=1}^{m}\frac{H(\mathbf{r})}{|\mathbf{r}_i-\mathbf{r}|}\frac{1}{t}\frac{\partial p_i(t)}{\partial t}\Big|_{t=T(\mathbf{r},\mathbf{r}_0)}, \tag{7}$$

where $T(\boldsymbol{r}, \boldsymbol{r}_0)$ is the corrected time of the acoustic wave propagating from $\boldsymbol{r}$ to $\boldsymbol{r}_0$,

$$T(\mathbf{r}, \mathbf{r}_0)\Big) = \frac{|\mathbf{r}-\mathbf{r}_0|}{c_0} - \Delta T(\mathrm{r}). \tag{8}$$

3. Results

3.1. Computer-simulated phantoms

We constructed computer-simulated phantoms of coronary arterial vessels and general biological cavities to validate the presented method. Fig. 2 shows the cross-sectional geometry of five examples. The tissue components, optical, acoustic and geometrical parameters are listed in Table 1 and Table 2 by referring to [32]. In the forward simulation, the sound speeds of each tissue component follow Gaussian distribution centered on the sound speeds listed in the tables. The source near-infrared (NIR) pulsed laser has a center wavelength of 1.7 μm and a pulse width of 20 ns by considering the strong absorption of the lipid in this wavelength and low laser energy required to distinguish the lipid from other tissue components [33]. The forward simulation and image reconstruction are implemented in MATLAB (R2016a, The MathWorks, Inc., Natick, Massachusetts).

3.2. Results of forward simulation

Fig. 3 shows the simulated PA signals of the vessel phantom 1# which were contaminated by Gaussian white noise with the signal-to-noise ratio (SNR) of 60 dB. In Fig. 3a, the four local peaks in the signal of $\theta = 0^\circ$ indicate the boundaries of the four layers in the direction of $\theta = 0^\circ$, while the two local peaks in the signal of $\theta = 180^\circ$ correspond to the boundaries of the two layers in the direction of $\theta = 180^\circ$ (Fig. 2a). Fig. 4 shows the transverse views of the acoustic pressure distribution images, where the lesions with the single and mixed component can be clearly distinguished.

3.3. Reconstruction results

In this section, the reconstruction results with our method are presented, where the initial sound speeds were set as $c_0 = 1450$ m/s, $c_1 = 1460$ m/s, $c_2 = 1470$ m/s, ..., $c_{20} = 1650$ m/s, $N = 20$ and $\Delta c = 10$ m/s. Fig. 5 shows the initial images of the optical absorption reconstructed from the simulated PA signals with a fixed initial SOS. Fig. 6 shows the linear curve of $\Delta T(\boldsymbol{r})$ relative to $H(\boldsymbol{r})$ fitted with three pairs of the temporal deviation and the radial depth, i.e., $\{(\Delta T(\boldsymbol{r}_1), H(\boldsymbol{r}_1)), (\Delta T(\boldsymbol{r}_2), H(\boldsymbol{r}_2)), (\Delta T(\boldsymbol{r}_3), H(\boldsymbol{r}_3))\}$, and M in eq. (6) was set as 3. Fig. 7 presents the finally recovered images.

4. Discussion

4.1. Evaluation of reconstruction quality

We used normalized mean square absolute distance (NMSAD) to quantitatively evaluate the reconstruction quality. NMSAD is defined as follows [34],

$$NMSAD = \frac{\sum_{u=1}^{S}\sum_{v=1}^{S}|y_{u,v}-x_{u,v}|}{\sum_{u=1}^{S}\sum_{v=1}^{S}y_{u,v}}, \tag{9}$$

where $x_{u,v}$ and $y_{u,v}$ are normalized intensities of the pixel (u, v) in the image X and Y. The image size is $S \times S$ pixels. Smaller NMSAD indicates more similar content of the two images. In our experiments, the image X and Y are the forward simulation image shown in Fig. 4 and the reconstructed image respectively. The results listed in Table 3 suggest that the reconstruction with our method is more accurate and closer to the forward simulation than the standard FBP reconstruction with a fixed SOS [31].

4.2. Evaluation of reconstruction accuracy

We located the plaques/lesions in the reconstructed curves of the initial acoustic pressure and compared the results with the forward simulation to evaluate the reconstruction accuracy. In Fig. 8, the plaques/lesions between two vertical solid lines, two vertical dotted lines and two vertical dashed lines are located by using the forward simulation, our method and the standard FBP method respectively. Obviously, the results of our method are closer to the forward simulation results than the standard FBP reconstruction. It indicates that the deviation of the ultrasonic propagation time caused by the variable SOS is effectively compensated. Thus, the tissue boundaries can be accurately located.

4.3. Computational time

The total time of reconstructing a cross-sectional grayscale image on a personal computer (PC) with an ADM A4-5000 1.5-GHz quad-core processor and a professional graphics workstation (GW) with an Intel i7-6700 k 4-GHz quad-core processor with hyper-threading is presented in Table 4. The results suggest that the time taken with our method is about 20 times as long as that with the standard FBP with a fixed SOS ($c = 1500$ m/s). This is because an iterative procedure inherently increases the computational time. As part of our future work, we aim to reduce this burden by using standard optimization techniques [27] to obtain faster recovery of the optical absorption density with the reconstruction process accelerated by means of graphics processing units (GPU) [35].

4.4. Dependence of reconstruction accuracy on initial sound speeds and temporal deviation

The above results were obtained in the case of $\Delta c = 10$ m/s and $M = 3$. In this section, the vessel phantom 1# is taken as an example to discuss the dependence of the reconstruction accuracy on Δc and M. In the case of $M = 3$, we changed Δc. When $\Delta c = 5$ m/s, total $N = 40$ initial sound speeds are set, i.e., $c_0 = 1450$ m/s, $c_1 = 1455$ m/s, $c_2 = 1460$ m/s, ..., $c_{40} = 1650$ m/s. Fig. 9 shows the initial acoustic pressure curve in the direction of $\theta = 1^\circ$ reconstructed with our method. In Fig. 9a, the location of the plaque/lesion between the two vertical solid lines, two vertical dotted lines and two vertical dashed lines is obtained by the forward simulation and our method where $\Delta c = 10$ m/s and $\Delta c = 5$ m/s respectively. Obviously, the results of $\Delta c = 5$ m/s are closer to the forward simulation. Table 5 lists the

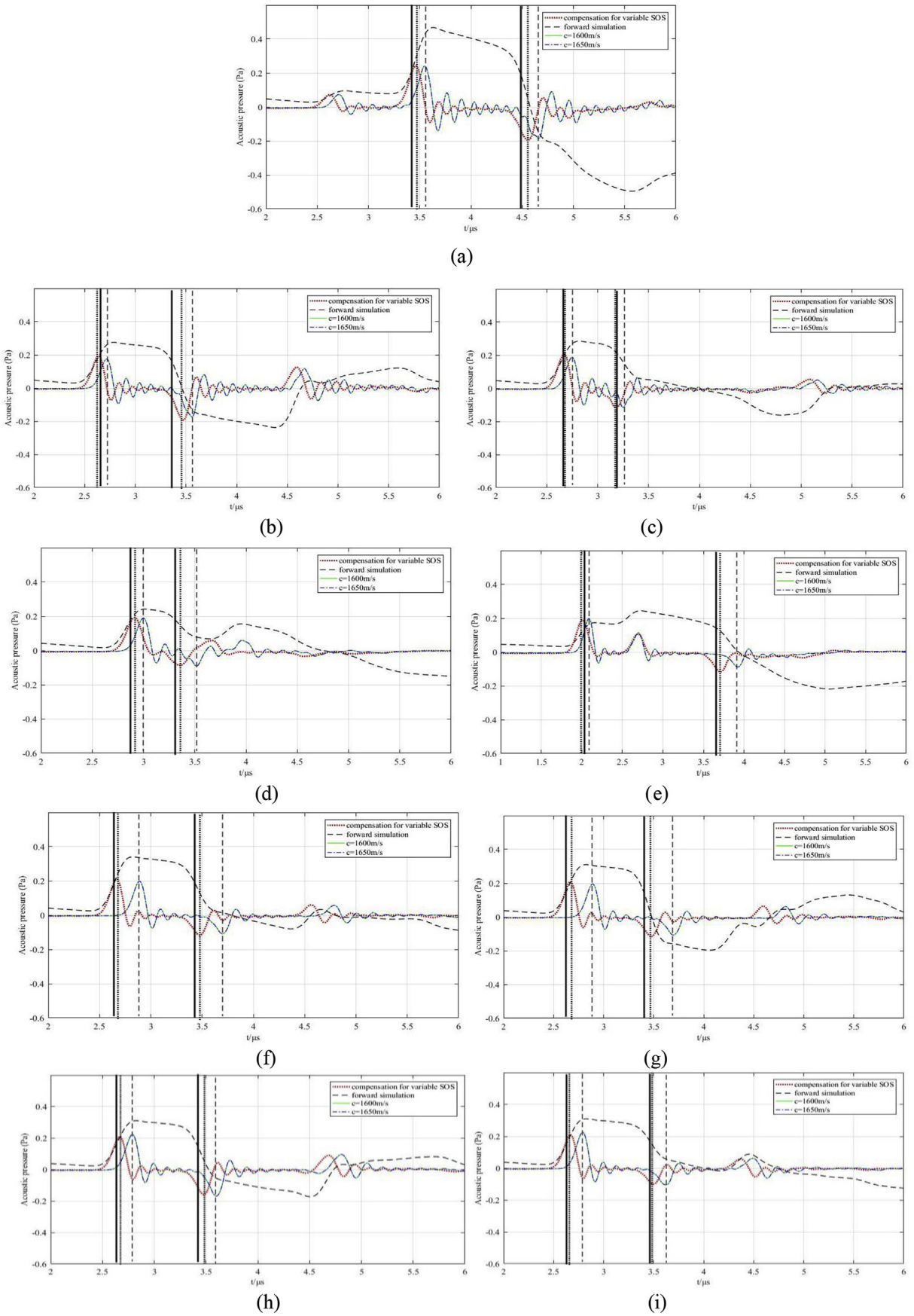

Fig. 8. Reconstructed normalized initial acoustic pressure curves. (a) Vessel 1# (θ = 1°); (b) Vessel 2# (θ = 1°); (c) Vessel 2# (θ = 180°); (d) Vessel 3# (θ = 45°); (e) Vessel 3# (θ = 180°); (f) Cavity 1#(θ = 3°); (g) Cavity 1# (θ = 245°); (h) Cavity 2# (θ = 1°); (i) Cavity 2# (θ = 158°).

Table 4
Time cost in reconstructing a cross-sectional image with a PC and a GW (Unit: *s*).

	Vessel 1#		Vessel 2#		Vessel 3#		Cavity 1#		Cavity 2#	
Our method	PC	GW	PC	GW	PC	GW	PC	GW	PC	GW
	376.156	142.373	393.349	164.344	378.304	149.017	388.155	156.551	389.124	160.329
Standard FBP	18.636	6.894	19.486	7.993	19.082	19.082	19.231	7.487	19.279	7.604

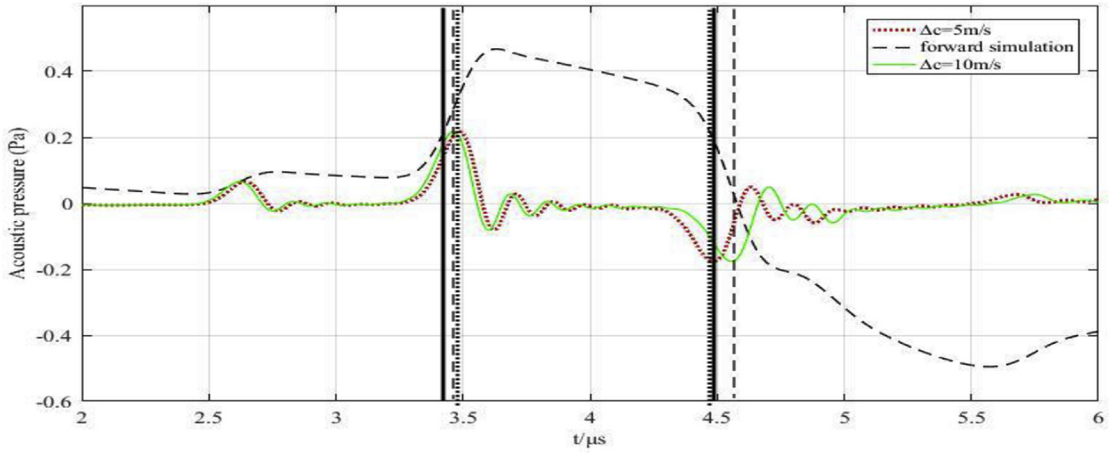

Fig. 9. Normalized initial acoustic pressure curves in the direction of $\theta = 1^{\circ}$ on the cross-section of vessel phantom 1#. (a) $\Delta c = 5$ m/s and 10 m/s ($M = 3$); (b) $M = 3$ and $M = 5$ ($\Delta c = 5$ m/s).

Table 5
NMSAD of images reconstructed with our method in case of different Δc and M for vessel phantom 1#.

Δc, M	NMSAD
$\Delta c = 10$ m/s, $M = 3$	4.754890
$\Delta c = 5$ m/s, $M = 3$	4.590642
$\Delta c = 5$ m/s, $M = 5$	4.681468

NMSADs of Fig. 10a and Fig. 7a. Here, we see the obvious reduction in NMSAD as Δc decreases. This is because a smaller Δc leads to a larger number of the initial sound speeds. Subsequently, it is more likely to choose the optimum at the cost of the computational time.

The results of $M = 5$ and $M = 3$ are compared as shown in Fig. 9b, where $\Delta c = 5$ m/s. In the figure, the plaques/lesions between the two vertical solid lines, two vertical dotted lines and two vertical dashed lines are located by using the forward simulation and our method where $M = 3$ and $M = 5$ respectively. Obviously, the results of $M = 5$ are closer to the forward simulation. From the NMSADs of Figs. 10b and 7a listed in Table 5, we see the obvious reduction in NMSAD as M increases. The reconstruction accuracy is closely related to the number of the temporal deviation values in different radial depths. More temporal deviation values lead to more accurate fitting and subsequently more accurate reconstruction. However, the computational cost is increased simultaneously.

4.5. Influence of noises in PA signals on reconstruction quality

We discussed the influence of the SNR of the PA signals on the reconstruction quality. The Gauss random noises were added to an acoustic pressure time series and Fig. 11 shows the reconstruction results of the cavity phantom 2# for different noise levels. The figure indicates that a higher SNR leads to a better reconstruction. The image

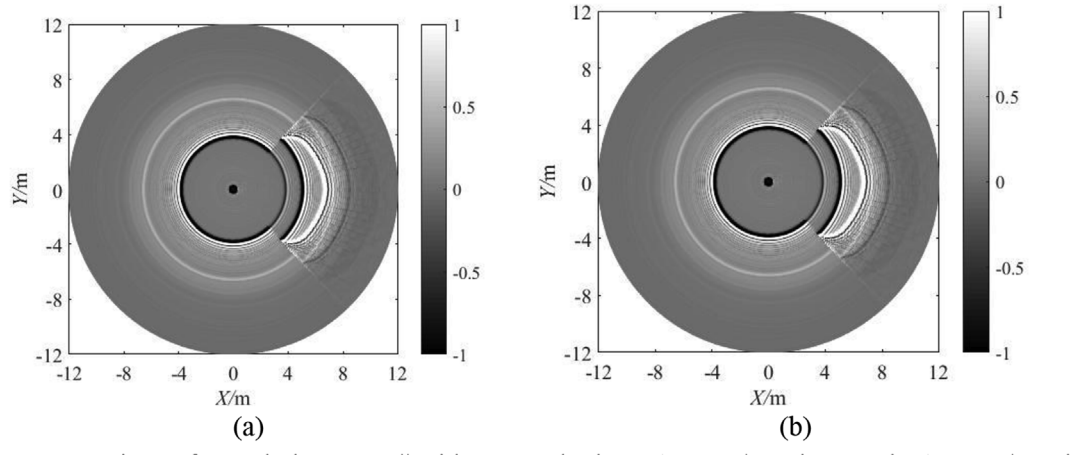

Fig. 10. Reconstructions of vessel phantom 1# with our method. (a) $\Delta c = 5$ m/s and $M = 3$; (b) $\Delta c = 5$ m/s and $M = 5$.

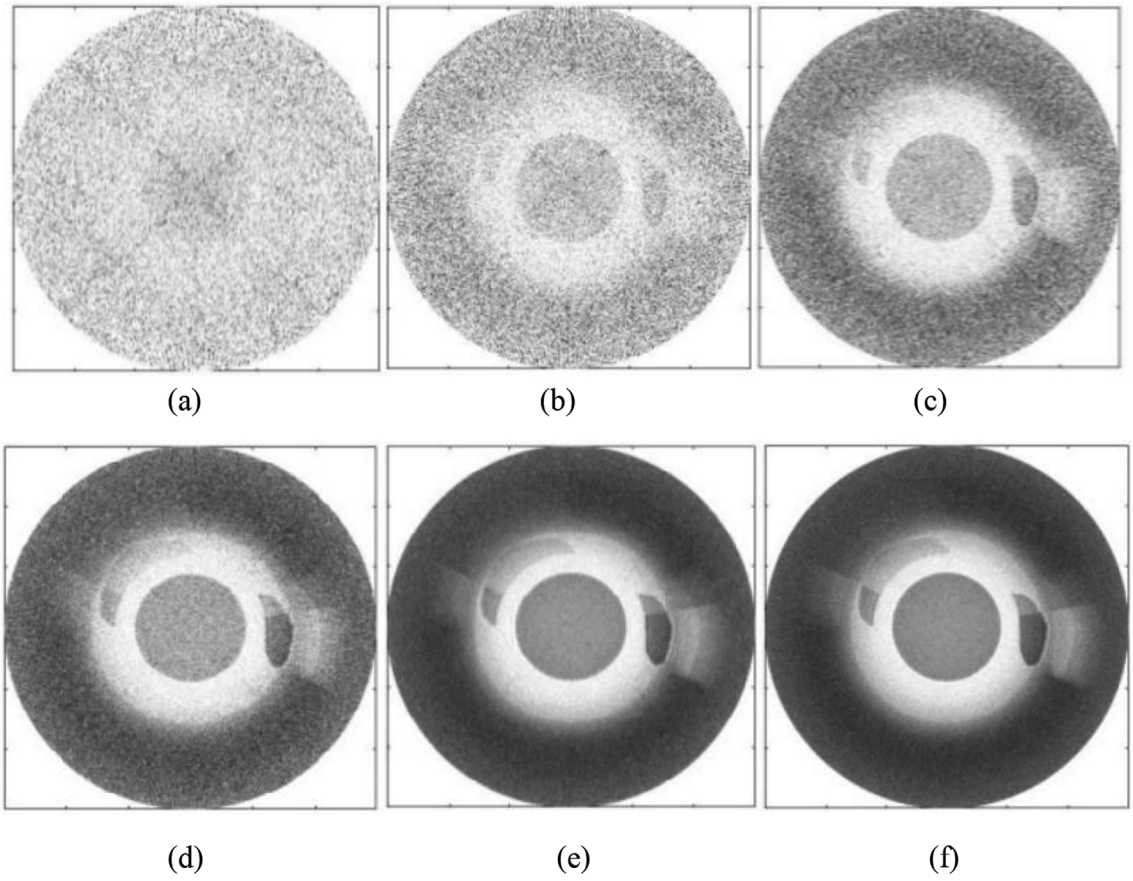

Fig. 11. Optical absorption distribution image of cavity phantom 2# for different noise levels. (a) SNR = 20 dB; (b) SNR = 30 dB; (c) SNR = 40 dB; (d) SNR = 50 dB; (e) SNR = 60 dB; (f) SNR = 70 dB.

quality is no longer improved obviously when SNR > 50 dB.

4.6. Comparison with optimal SOS group method

We compared the reconstructions obtained with our method and the optimal SOS group method presented in [19,20]. Fig. 12 shows the results of the vessel phantom 1# obtained with the optimal SOS group method, where the initial SOS group was set as listed in Table 6. Table 7 lists the NMSADs and the time cost of Figs. 12 and 7a. From the table, we see the obviously higher time cost of the optimal SOS group method in comparison to our method although its NMSAD is somewhat lower.

The accuracy of the optimal SOS group method highly depends on the initial SOS group. The prior knowledge about the internal structure of the imaged target is usually necessary to achieve satisfied reconstruction. Therefore, the optimal SOS group method is applicable to an ultrasonic-photoacoustic (USPA) dual-modal combined imaging system, where the US and PA measurement can be acquired simultaneously. Thus, the initial SOS group can be set according to the US measurement.

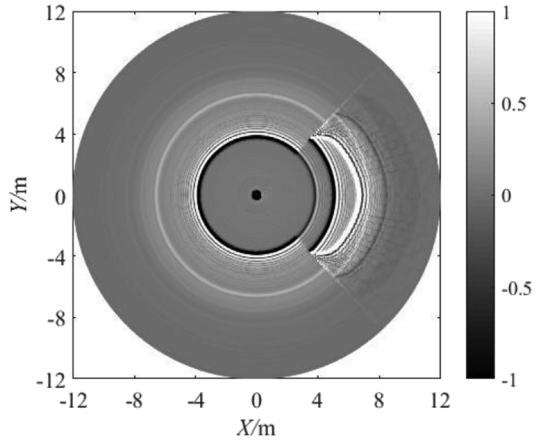

Fig. 12. Reconstruction of vessel phantom 1# by using the optimal SOS group method.

Table 6
Initial SOS group for vessel phantom 1# set in the optimal SOS group method.

Tissue name	Composition	SOS (*m/s*)
Intima/Media	Muscular tissue	1568
Adventitia	Connective tissue	1613
Lumen	Blood	1580
Calcified plaque	Calcium	2770

Table 7
NMSAD and time cost of the optimal SOS group method and our method.

Method	NMSAD	Time cost (*s*)
Optimal SOS group	4.483021	894.5472
Our method	4.754890	376.1562

5. Conclusion

In this paper, an image reconstruction method is designed and implemented. It is suitable for EPAT of the soft tissues of luminal structures with variable SOS, such as coronary arteries or digestive tracts, where the SOS ranges from 1450 m/s to 1650 m/s and the variation in SOS is lower than 10%. Neither additional equipment to be used to measure the SOS distribution nor the prior knowledge of the SOS distribution is required. Any assumptions on the target size and the geometry as well as the distance from the ultrasonic detector to the target are not needed. The computer-simulation demonstrations suggest that the target misalignment and acoustic distortion in the reconstructed images caused by the variable SOS are effectively corrected. The reconstruction accuracy can be improved by reducing the step of the initial SOS and increasing the number of the temporal deviation values at the cost of increasing the computational cost. Results of comparison experiments indicate that both the optimal SOS group method and our method can effectively improve the reconstruction quality. However, the optimal SOS group method highly depends on the manually set initial SOS group and the prior knowledge about the internal structure of the target is usually necessary. So, it is suitable for USPA dual-modal imaging instead of EPAT single-modal imaging.

Conflicts of interest

None Declared.

Acknowledgments

This work was supported by National Natural Science Foundation of China(no. 61372042).

References

[1] Y. Li, Z. Chen, Multimodal intravascular photoacoustic and ultrasound imaging, Biomed. Eng. Lett. 8 (2) (2018) 193–201.
[2] K. Xiong, S. Yang, X. Li, D. Xing, Autofocusing optical-resolution photoacoustic endoscopy, Optic Lett. 43 (8) (2018) 1846.
[3] R. Ansari, E.Z. Zhang, A.E. Desjardins, P.C. Beard, All-optical forward-viewing photoacoustic probe for high-resolution 3D endoscopy, Light Sci. Appl. 7 (2018) 75.
[4] Z. Sun, D. Han, Y. Yuan, 2-D image reconstruction of photoacoustic endoscopic imaging based on time-reversal, Comput. Biol. Med. 76 (2016) 60–68.
[5] T. Vu, Y. Wang, J. Xia, Optimizing photoacoustic image reconstruction using cross-platform parallel computation, Vis. Comput. Ind. Biomed. Art 1 (2018) 2.
[6] Z. Sun, L. Zheng, Reconstruction of optical absorption coefficient distribution in intravascular photoacoustic imaging, Comput. Biol. Med. 97 (2018) 37–49.
[7] Z. Sun, D. Han, J. Wang, Review of image reconstruction for intravascular photoacoustic imaging, Opto-Electronic Eng. 42 (3) (2015) 20–27.
[8] J. Xia, C. Huang, K. Maslov, et al., Enhancement of photoacoustic tomography by ultrasonic computed tomography based on optical excitation of elements of a full-ring transducer array, Optic Lett. 38 (16) (2013) 3140.
[9] Y. Xu, D. Feng, L.V. Wang, Exact frequency-domain reconstruction for thermoacoustic tomography-I:planar geometry, IEEE Trans. Med. Imaging 21 (7) (2002) 823–828.
[10] C. Yoon, J. Kang, S. Han, et al., Enhancement of photoacoustic image quality by sound speed correction: ex vivo evaluation, Optic Express 20 (3) (2012) 3082–3090.
[11] J. Zhang, M.A. Anastasio, Reconstruction of speed-of-sound and electromagnetic absorption distributions in photoacoustic tomography, Proceedings of Photons Plus Ultrasound: Imaging and Sensing 2006: the Seventh Conference on Biomedical Thermoacoustics, Optoacoustics, and Acousto-Optics, 6 Mar, vol. 6086, 2006, p. 608619.
[12] J. Zhang, K. Wang, Y. Yang, M.A. Anastasio, Simultaneous reconstruction of speed-of-sound and optical absorption properties in photoacoustic tomography via a time-domain iterative algorithm, Proceedings of Photons Plus Ultrasound: Imaging and Sensing 2008: the Ninth Conference on Biomedical Thermoacoustics, Optoacoustics, and Acousto-Optics, 28 Feb, vol. 6856, 2008, p. 68561F.
[13] X. Jin, L.V. Wang, Thermoacoustic tomography with correction for acoustic speed variations, Phys. Med. Biol. 51 (24) (2006) 6437–6448.
[14] J. Xia, C. Huang, K. Maslov, et al., Enhancement of photoacoustic tomography by ultrasonic computed tomography based on optical excitation of elements of a full-ring transducer array, Opt. Lett. 8 (9) (2013) 3140–3143.
[15] C. Zhang, Y. Wang, A reconstruction algorithm for thermoacoustic tomography with compensation for acoustic speed heterogeneity, Phys. Med. Biol. 53 (18) (2008) 4971–4982.
[16] Y. Zhu, W. Li, L. Zhang, et al., Reconstruction in photoacoustic tomography based on fitted delay compensation, Opto-Electronic Eng. 42 (4) (2015) 56–61.
[17] B.E. Treeby, T.K. Varslot, E.Z. Zhang, et al., Automatic sound speed selection in photoacoustic image reconstruction using an autofocus approach, J. Biomed. Opt. 16 (9) (2011) 090501.
[18] B. Cong, K. Kondo, T. Namita, et al., Photoacoustic image quality enhancement by estimating mean sound speed based on optimum focusing, Jpn. J. Appl. Phys. 54 (7S1) (2015) 07HC13.
[19] M. Ye, M. Cao, T. Feng, et al., Automatic speed of sound correction with photoacoustic image reconstruction, Proceedings of SPIE International Conference on Photons Plus Ultrasound: Imaging and Sensing. 15 March, vol. 9708, 2016, p. 97083D.
[20] M. Ye, J. Yuan, The study of selecting the optimal SOS group based on PA imaging, J. Nanjing Univ. (Nat. Sci.) 52 (3) (2016) 528–535.
[21] J. Wang, Z. Zhao, J. Song, et al., Reconstruction of microwave absorption properties in heterogeneous tissue for microwave-induced thermo-acoustic tomography, Prog. Electromagn. Res. 130 (19) (2012) 225–240.
[22] J. Wang, Z. Zhao, J. Song, et al., Reducing the effects of acoustic heterogeneity with an iterative reconstruction method from experimental data in microwave induced thermoacoustic tomography, Med. Phys. 42 (5) (2015) 2103–2112.
[23] J. Wang, Z. Zhao, J. Song, et al., Iterative reconstruction method with optimal time-of-flights for imaging microwave absorption properties of tissues in acoustically heterogeneous environment in microwave-induced thermoacoustic tomography (MITAT), J. Electromagn. Waves Appl. 28 (18) (2014) 2350–2363.
[24] C. Huang, K. Wang, L. Nie, et al., Full-wave iterative image reconstruction in photoacoustic tomography with acoustically inhomogeneous media, IEEE Trans. Med. Imaging 32 (6) (2013) 1097–1110.
[25] A. Javaherian, S. Holman, A multi-grid iterative method for photoacoustic tomography, IEEE Trans. Med. Imaging 36 (3) (2017) 696–706.
[26] M. Haltmeier, L.V. Nguyen, Analysis of iterative methods in photoacoustic tomography with variable sound speed, SIAM J. Imag. Sci. 10 (2) (2017) 751–781.
[27] G. Zangerl, M. Haltmeier, L.V. Nguyen, et al., Full Field Inversion in Photoacoustic Tomography with Variable Sound Speed, (2018), p. 00816 arXiv:1808.
[28] H. Zhang, S. Chen, J. Wang, The matrix transform for reconstruction on finite-element-based photoacoustic tomography, J. Comput. Commun. 04 (3) (2016) 54–60.

[29] Z. Belhachmi, T. Glatz, O. Scherzer, A direct method for photoacoustic tomography with inhomogeneous sound speed, Inverse Probl. 32 (4) (2016) 045005.
[30] C. Huang, K. Wang, R.W. Schoonover, et al., Joint reconstruction of absorbed optical energy density and sound speed distributions in photoacoustic computed tomography: a numerical investigation, IEEE Trans. Comput. Imaging 2 (2) (2016) 136–149.
[31] Z. Sun, Y. Yuan, D. Han, A computer-based simulator for intravascular photoacoustic images, Comput. Biol. Med. 81 (2017) 176–187.
[32] S.L. Jacques, Optical properties of biological tissues: a review, Phys. Med. Biol. 58 (11) (2013) R37.
[33] S.J. Mathews, C. Little, C.D. Loder, et al., All-optical dual photoacoustic and optical coherence tomography intravascular probe, Photoacoustics 11 (2018) 65–70.
[34] Z. Sun, Z. Ma, Numerical simulation of endoscopic magnetoacoustic tomography with magnetic induction, Comput. Biol. Med. 90 (2017) 1–14.
[35] T. Shan, H. Jiang, Accelerated time domain quantitative photoacoustic tomography (TD-qPAT) based on graphic processing units (GPU) for clinical application of breast cancer imaging, Proceedings of OSA (Optical Society of America) Biophotonics Congress: Biomedical Optics Congress, 2018 Hollywood, Florida United States, 3–6 April 2018, paper OW4D.3.